

# Faradaic effects in electrochemically gated graphene sensors in the presence of redox active molecules

Tilmann J Neubert<sup>1,2</sup> , Michel Wehrhold<sup>1</sup> , Nur Selin Kaya<sup>1</sup>  
and Kannan Balasubramanian<sup>1</sup> 

<sup>1</sup> School of Analytical Sciences Adlershof (SALSA), IRIS Adlershof and Department of Chemistry, Humboldt-Universität zu Berlin, Berlin, Germany

<sup>2</sup> Institut für Silizium-Photovoltaik, Helmholtz-Zentrum Berlin für Materialien und Energie GmbH, Berlin, Germany

E-mail: [tilmann.neubert@hu-berlin.de](mailto:tilmann.neubert@hu-berlin.de) and [nano.anchem@hu-berlin.de](mailto:nano.anchem@hu-berlin.de)

Received 4 May 2020, revised 13 May 2020

Accepted for publication 2 June 2020

Published 14 July 2020



## Abstract

Field-effect transistors (FETs) based on graphene are promising devices for the direct sensing of a range of analytes in solution. We show here that the presence of redox active molecules in the analyte solution leads to the occurrence of heterogeneous electron transfer with graphene generating a Faradaic current (electron transfer) in a FET configuration resulting in shifts of the Dirac point. Such a shift occurs if the Faradaic current is significantly high, e.g. due to a large graphene area. Furthermore, the redox shift based on the Faradaic current, reminiscent of a doping-like effect, is found to be non-Nernstian and dependent on parameters known from electrode kinetics in potentiodynamic methods, such as the electrode area, the standard potential of the redox probes and the scan rate of the gate voltage modulation. This behavior clearly differentiates this effect from other transduction mechanisms based on electrostatic interactions or molecular charge transfer doping effects, which are usually behind a shift of the Dirac point. These observations suggest that large-area unmodified/pristine graphene in field-effect sensors behaves as a non-polarized electrode in liquid. Strategies for ensuring a polarized interface are discussed.

Supplementary material for this article is available [online](#)

Keywords: graphene, redox, field-effect, electron transfer, Faradaic current, sensor

(Some figures may appear in colour only in the online journal)

## 1. Introduction

Analytical graphene devices are emerging as versatile electronic platforms for chemical sensing and biosensing [1–4]. In addition to enabling the detection of analyte species down

to low concentrations, they facilitate the investigation of fundamental processes at the nanoscale graphene-liquid-interface (GLI) [5, 6]. Based on the measurement strategy, these reports can be broadly classified into two categories: graphene sensing platforms in a field-effect transistor (FET) configuration operating in liquids (GFETs) and electrochemical (EC) sensors, where a single graphene sheet is employed as the working electrode (WE) as part of an electrochemical cell [7, 8]. GFET sensors have been reported for the detection of various analyte species, including enzymes [9], antibodies [10], DNA [11–13] and others [2, 4, 14, 15]. In many of these examples, the graphene surface is functionalized with appropriate receptor



Original content from this work may be used under the terms of the [Creative Commons Attribution 4.0 licence](#). Any further distribution of this work must maintain attribution to the author(s) and the title of the work, journal citation and DOI.

molecules to achieve selectivity towards an analyte of interest. Unmodified or pristine graphene devices serve the study of fundamental interfacial processes [5, 6, 16–18], as well as the realization of novel detection schemes [19, 20]. In electrochemical studies, the kinetics of electron transfer (ET) with a range of redox active species has been in focus at pristine graphene WEs [21–26]. Also, in this configuration, new kinds of sensors have been demonstrated [27].

One of the fundamental challenges in the area of nanostructure-based sensors is the understanding of the transduction mechanism behind the observed sensor responses [2, 6, 28]. Among the various mechanisms proposed, two principal pathways are the most common. In the first case, local changes in electrostatic charge distribution at the nanostructure-liquid-interface lead to a threshold voltage shift or doping in the observed FET transfer characteristics. This is analogous to an additional electrostatic gate at the interface. Secondly, the adsorption of analytes may induce charge transfer between the nanostructure and the analyte molecules resulting in a threshold voltage shift and a change in graphene resistance and charge carrier mobility [29–31]. Other effects, such as Schottky barrier modulation, can be minimized by passivating the graphene contacts with an appropriate insulator [2, 32].

These mechanisms apply equally for GFET sensors operating in liquid, where a reference electrode (RE) in contact with the solution is used as a gate [2, 28]. Here, it is often assumed that the GLI behaves as a polarized interface, where negligible currents flow between the RE/gate and the graphene electrode. Such leakage currents, if present, are typically capacitive and non-Faradaic. The widely deployed FET configuration in liquid with the RE as the gate is in principle identical to a two-electrode electrochemical cell [5, 33]. An alternative configuration that ensures no polarization of the RE involves the use of an electrochemical potentiostat to control the gate voltage [34, 35]. From EC measurements, it is known that ET reactions do occur at pristine graphene electrodes with appropriate redox active species in solution causing Faradaic currents [21, 25, 36]. This is in contrast to bulk semiconductor-based ion-selective FETs (ISFETs) introduced in the 1970s [37], where ET typically does not occur (at least directly) between the semiconductor channel and molecules in solution [38], due to the presence of an intermediate insulating layer. It has been theoretically suggested that in the presence of redox active species in solution, ET reactions occurring at the GLI may modulate the interfacial potential and hence render the direct detection of charges difficult [39]. Since the detection of charges is an important transduction mechanism in (bio)sensing based on field-effect measurements, understanding and avoiding ET at the GLI is important for the design of such biosensors.

In back-gated GFET devices and non-contacted graphene, it was proposed that the  $O_2/H_2O$  redox couple is behind the commonly observed *p*-doping effect [18, 40]. The electrochemical reduction of  $O_2$  leads to reactive species (e.g.  $O_2^{\bullet-}$ ,  $H_2O_2$ ,  $\bullet OH$ ), which are strong Brønsted bases fixing net negative charges on the surface of graphene and trapping holes, explaining the observed *p*-doping effect. In

electrochemical GFETs operating in liquid such an effect has not been reported yet. With single-walled carbon nanotube (SWNT) FETs, a shift of the threshold voltage has been observed due to charge transfer in the presence of the redox active probes hexachloroiridate(III)/(IV)  $[IrCl_6]^{2-/3-}$  and hexacyanoferrate(II)/(III)  $[Fe(CN)_6]^{3-/4-}$  [41].

Also, from a fundamental electrochemical perspective, the study of the interaction of redox probes with graphene is an interesting prospect. In metal electrodes used to interrogate redox probes, the occurrence of interfacial ET does not affect the electronic filling level of the underlying electrode. In marked contrast to this, monolayer graphene electrodes are characteristic of a low density of states [5, 18]. Due to the unique electronic structure of graphene, ET with redox active molecules is expected to modify the filling level in the graphene electrode. The Marcus–Gerischer theory has been applied to model ET processes in graphene and SWNTs [5, 18, 33]. The density of states (DOS) of the carbon electrode material and the redox states of the species in solution have been compared to explain how the overlap of states influences the direction and efficiency of the charge transfer process. While there are several reports on the effects of the electronic structure of graphene on the rates of electrochemical processes [5, 36, 42, 43], the effect of interfacial heterogeneous ET on the observed field-effect characteristics has seldom been studied systematically.

This study is aimed at addressing this gap. Through correlated field-effect measurements and electroanalysis, we corroborate the effect of the canonical redox probes  $[IrCl_6]^{2-/3-}$  and  $[Fe(CN)_6]^{3-/4-}$  as model charge transfer analytes on the electronic properties of graphene as observed by the field-effect in liquids with an Ag/AgCl RE as the gate. Depending on the formal potential  $E^0$  of the redox couples, shifts akin to *p*-doping are observed. By investigating the characteristics of this effect in detail, we show that the observed phenomenon is unique for redox active molecules interacting with graphene in an electrochemically gated configuration.

## 2. Results and discussion

### 2.1. Correlation between Faradaic current and the Dirac point shift

First, we focus on the interactions of the probe  $[IrCl_6]^{2-/3-}$  with graphene measured by the field-effect and electroanalysis. Graphene devices were fabricated with CVD-grown monolayer graphene as the conduction channel, between two Ti/Pt electrodes on Si/SiO<sub>2</sub> substrates. (See section 4 and the supporting information (SI) for details of the fabrication process (with flow chart—figure S1 (available online at [stacks.iop.org/NANO/31/405201/mmedia](https://stacks.iop.org/NANO/31/405201/mmedia)) in the SI) and measurement configuration.) Shortly, graphene was transferred using a metal-ion-free wet transfer strategy followed by removal of trace impurities using electrochemical etching [21, 44] and annealing. The contacts are passivated using an SU-8 (10 μm) photoresist. The final graphene area  $A_{Gr}$  is 1.1 mm<sup>2</sup>. Representative optical images and Raman spectra of a graphene device are shown in figure S2 in the SI. The

field-effect is measured in liquids by recording the real part of impedance (at a constant frequency) of the contacted graphene layer as a function of the gate voltage ( $V_{\text{ecG}}$ , ecG: electrochemical gate) continuously in various solutions. The use of an AC signal to measure the GFET channel resistance eliminates the occurrence of parasitic leakage currents in the drain current channel. The gate voltage is applied through an Ag/AgCl (3 M KCl) RE that is in contact with the solution. Figures 1(a) and (b) present maps [6, 9] of the evolution of the field-effect for a typical graphene sheet (size approx. 1.1 mm<sup>2</sup>) in buffer when exposed to increasing concentrations of the oxidized form  $[\text{IrCl}_6]^{2-}$  and reduced form  $[\text{IrCl}_6]^{3-}$ , respectively. Gate voltage scans at selected cycles are shown in figure 1(c), from where the Dirac point ( $V_{\text{Dirac}}$ , the value of  $V_{\text{ecG}}$  where the resistance is maximum) can be extracted. The Dirac point values for every cycle are also indicated in white in the field-effect maps in figures 1(a) and (b). It is apparent that with increasing concentration of the oxidized species  $[\text{IrCl}_6]^{2-}$  the Dirac point shifts to higher values, while negligible changes are observed when the reduced species  $[\text{IrCl}_6]^{3-}$  is increasingly present in solution. This is further clear in the plot of the shift in the Dirac point ( $\Delta V_{\text{Dirac}}$ ) as a function of concentration shown in figure 1(d), which appears to be linearly proportional to the concentration of oxidized species. Electrostatic interactions can be ruled out as being the reason behind this shift, since in this case the shift (or the  $p$ -doping effect) should be larger for the reduced species  $[\text{IrCl}_6]^{3-}$  due to the higher charge. Additionally, the shift of the Dirac point should be observed as a linear function of the analyte concentration on a logarithmic scale, which is not the case here.

To shed more light on the observed behavior, cyclic voltammetry (CV) with  $[\text{IrCl}_6]^{2-/3-}$  was carried out on a graphene device, which is shown in figure 2(a) along with the gate dependence of conductance for the same device in the same buffer. The CV was measured using the contacted graphene as the WE in a three-electrode cell with a Pt counter electrode and a Ag/AgCl (3 M KCl) RE. To be able to compare the two measurements on the same scale, the electrochemical current (red curve) is plotted against the potential at the RE, instead of the usual electrochemical convention of using the potential of the WE versus the reference ( $E_{\text{appl}}$ ). In field-effect measurements, the gate voltage  $V_{\text{ecG}}$  is applied via the same RE as in the CVs, and hence  $V_{\text{ecG}} = -E_{\text{appl}}$ . We will use the  $V_{\text{ecG}}$  scale to present all the EC data hereafter. From this figure, it is clear that the formal potential of the redox couple  $[\text{IrCl}_6]^{2-/3-}$  ( $E^{0'}$ ) lies well within the hole carrier regime (or valence band) of graphene. Hence, the voltage range where the field-effect is measured occurs at highly cathodic potentials with respect to the  $E^{0'}$  of the  $[\text{IrCl}_6]^{2-/3-}$  couple. As a result, when the oxidized form  $[\text{IrCl}_6]^{2-}$  is introduced, ET from graphene occurs causing the reduction of  $[\text{IrCl}_6]^{2-}$ , while the reduced form does not introduce any ET. ET between redox probes and graphene is often explained by the Marcus–Gerischer model with the distribution of states for the oxidized ( $D_{\text{ox}}$ ) and reduced ( $D_{\text{red}}$ ) species and comparing it with the graphene electronic structure on the  $V_{\text{ecG}}$  scale, as shown schematically in figure 2(b) [18, 45]. The shift in the Dirac point observed for  $[\text{IrCl}_6]^{2-}$  correlates with the

filling of the empty  $D_{\text{ox}}$  states by the heterogeneous transfer of electrons from graphene during the gate modulation. In contrast,  $[\text{IrCl}_6]^{3-}$  cannot accept electrons, since the  $D_{\text{red}}$  states are filled already when scanning in the gate voltage range of the field-effect. The linear shift in the Dirac point as a function of concentration, as mentioned above, is consistent with the fact that the density of states  $D_{\text{ox}}$  ( $[\text{IrCl}_6]^{2-}$ ) increases linearly as a function of the concentration [45]. However, during the gating experiment, ET continuously occurs. Based on the above model, one would expect a dynamic behavior here, wherein the Dirac point should shift continuously over time as charge transfer occurs, as has been reported for back-gated and non-gated samples [18, 40]. This is not what we observe though, i.e. the shift is constant for a given concentration of reduced species.

To identify the cause of this peculiar behavior in our measurement configuration, we have recorded the current flowing between the Ag/AgCl gate electrode and graphene in the deployed gate voltage range. This configuration is identical to a two-electrode CV measurement performed in the absence of a counter electrode. Figures 3(a) and (b) present such two-electrode CVs (for the device in figure 1) in varying concentrations of oxidized and reduced species along with the data for the same measurement in blank buffer (black curves). The magnitude of the cathodic/reductive current increases with the concentration of  $[\text{IrCl}_6]^{2-}$  (figure 3(a)), while it remains at the level of the blank buffer solution for all concentrations of  $[\text{IrCl}_6]^{3-}$  (figure 3(b)). (See figure S3 for the complete CVs.) This is consistent with the previous explanation that in the probed voltage range, only the oxidized species undergoes reduction via ET. Based on these data, it is clear that there is a current flowing between the gate and the graphene channel, which is additionally caused by the reduction of the oxidized species. This Faradaic (reductive) current may be behind the observed shifts in the Dirac point, since there is a clear correlation between the two, as shown in figure 3(c). The Faradaic current is known to be directly proportional to the concentration of the redox probe [45]. Accordingly, the Dirac point shift (figure 1) is found to be linearly dependent on the concentration of the oxidized species and is fundamentally different from typical transduction mechanisms described for GFET sensors. Since the shift is caused by a Faradaic current, we refer to it as a *Faradaic effect*.

## 2.2. The non-polarized nature of the GLI

It is worth mentioning that this current is distinctly different from a leakage current that typically constitutes a parasitic effect. In blank buffer, an electrochemical current is indeed flowing between the gate and graphene. However, this is a non-Faradaic background current due to the double layer capacitance and electrolyte resistance, which is not affecting the potential of the deployed RE and the measurement of the graphene field-effect itself (see figure S4 in the SI for the stability of the gate response and figure S5 for the stability of the RE potential). It is clear that the observed Dirac point shift is due to an *additional* Faradaic current coming exclusively from ET with the oxidized species  $[\text{IrCl}_6]^{2-}$  at the GLI on top

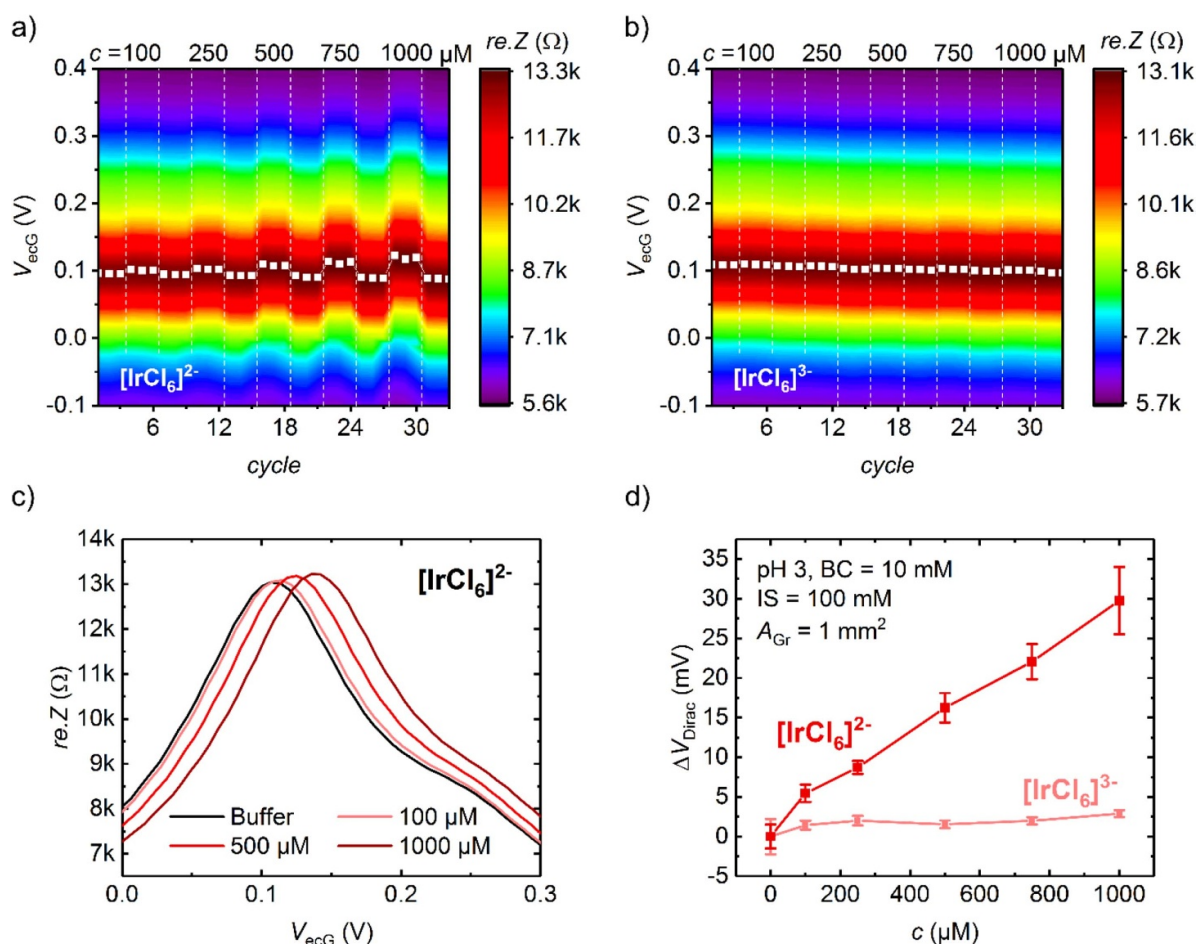


**Figure 1.** The field-effect response of graphene in the presence of  $[\text{IrCl}_6]^{2-/3-}$  redox probes. (a), (b) Evolution of the gate dependence of resistance ( $re.Z$ ) in blank buffer with increasing concentration of the redox probes (a: oxidized  $[\text{IrCl}_6]^{2-}$ ; b: reduced  $[\text{IrCl}_6]^{3-}$ ), plotted as a 2D map. In every cycle ( $X$ -axis), the resistance ( $Z$ -axis) measured as a function of gate voltage ( $Y$ -axis) is plotted as a color map. The first three cycles are measured in buffer, the following three with 100  $\mu\text{M}$  probe in the same buffer and so on. The concentration values are shown on top of the map. The white profile indicates the position of the Dirac point (maximum resistance in every cycle) (c) selected individual cycles from the map in (a), from where the Dirac point is extracted. Note that figure (a) can be understood as a bird's-eye view of figure (c), with the advantage of directly comparing consecutive cycles of the measurement. (d) Evolution of the shift in the Dirac point  $\Delta V_{Dirac}$  (with respect to the Dirac point in blank buffer) as a function of the concentration of  $[\text{IrCl}_6]^{2-}$  and  $[\text{IrCl}_6]^{3-}$ . The measurements were performed in phosphate buffer at pH 3 (buffer concentration (BC) 10 mM, ionic strength (IS) 100 mM). The area of the graphene  $A_{Gr}$  is 1.1  $\text{mm}^2$ .

of the background current. As shown in figure 3, the Faradaic current surpasses the background current by far. If it was just a parasitic leakage current, for example, due to higher electrolyte conductivity for increasing concentrations, this should be observed for both forms of the redox probe. This is, however, not the case here.

Secondly, in the presence of heterogeneous ET at the graphene electrode, this current will occur if a proper RE is used as a gate. This is because the RE in the ideal case is a non-polarized electrode and will allow a low level of Faradaic redox current ( $\text{Ag}/\text{AgCl}/\text{Cl}^\ominus$  half cell) to flow with little changes in its electrode potential [45, 46]. The commonly used  $\text{Ag}/\text{AgCl}$  electrode is able to allow the passage of currents in the presence of a sufficient amount of chloride ions in solution according to the reaction:  $\text{AgCl} + e^\ominus \rightarrow \text{Ag} + \text{Cl}^\ominus$ . However, in a typical three-electrode electrochemical setup, the passage of current at a RE is nearly completely suppressed electronically (high input impedance, when using a potentiostat), ensuring

that the potential of the  $\text{Ag}/\text{AgCl}$  RE remains constant during the measurement. In contrast, in a simple two-electrode FET setup typically there is no electronic control over the gate-channel current. Hence, when a reduction is forced at the GLI due to the applied voltage range, a corresponding oxidation occurs at the RE generating a Faradaic current.

It could be argued that the Faradaic current leads to a polarization of the non-ideal  $\text{Ag}/\text{AgCl}$  RE, which might be the cause of the observed Dirac point shift in a two-electrode FET setup (figure 4(a)). The polarization of the RE can be avoided electronically by using an electrochemical potentiostat to control the applied gate voltage, as shown in the schematic in figure 4(b). In this measurement configuration, the Faradaic current occurring at the GLI is compensated by the counter electrode. This avoids any current flow at the RE, ensuring a constant reference potential at the  $\text{Ag}/\text{AgCl}$  electrode. In this configuration, the resistance of the graphene channel is measured using a lock-in amplifier simultaneously when the

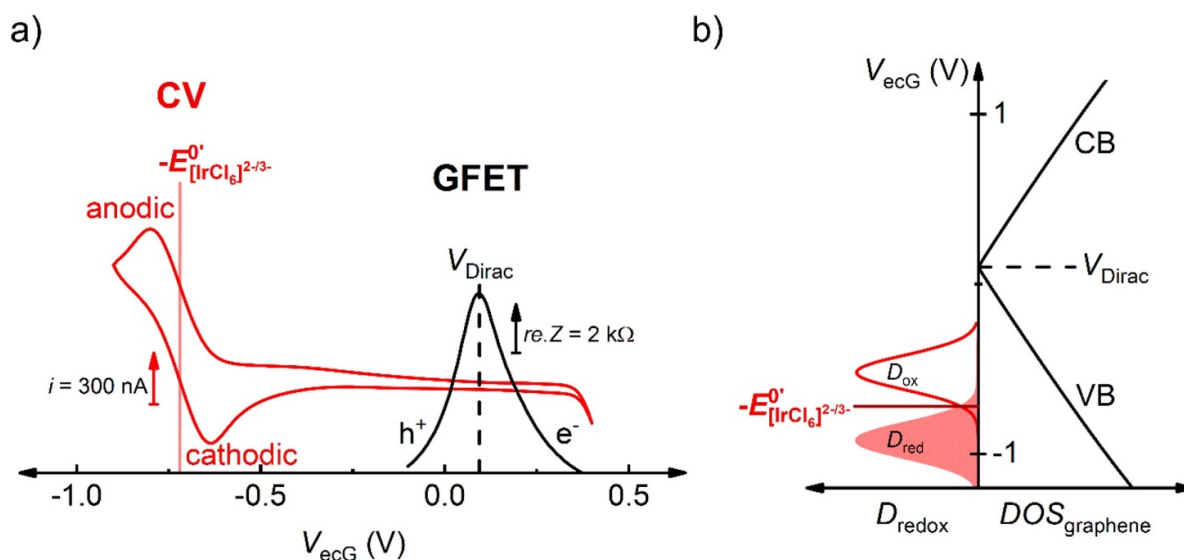


**Figure 2.** (a) Comparison of the CV of  $[IrCl_6]^{2-/3-}$  (0.5 mM) at the graphene WE (red curve) and the gate dependence of the resistance of graphene (black curve) in blank buffer. Both curves are plotted as current/resistance as a function of voltage at the RE ( $V_{ecG}$ ). (b) Alignment of the graphene density of states  $DOS_{graphene}$  against the distribution of redox states  $D_{red}/D_{ox}$  of  $[IrCl_6]^{2-/3-}$  around its formal standard potential  $E^{0'}$  in accordance with the Marcus–Gerischer model. Here,  $V_{Dirac}$  and  $E^{0'}$  have been extracted from the measurements displayed in (a). See figure S3(c) for an absolute scale of the data in (a).

electrochemical potential is modulated using a potentiostat (see the experimental section for details of the measurement setup). Figures 4(c) and (d) compare the evolution of the Dirac point shift measured using such a setup with respect to the standard two-electrode FET setup. It is apparent that, in this case, a clear shift in the Dirac point is also observed, however of a lower magnitude. While a certain polarization of the Ag/AgCl appears to occur in the commonly used two-electrode FET setup, it is clear that the observed shift in the Dirac point is at least partly due to the Faradaic current at the GLI. Further confirmation is obtained by area-dependent measurements discussed later. It should be noted that this polarization in graphene is not caused by an improper device configuration or an unstable RE, but rather by the presence of the redox molecule (or analyte) itself. It is worth mentioning that currents of this strength should be avoided at the RE in the two-electrode setup. Over time, these currents may lead to corrosion of the electrode and thereby change its potential permanently. We have evaluated the stability of the used RE by calibration against another unused RE between the measurements. The open circuit potential ( $E_{OCP}$ ) between the two electrodes remained in the range of  $E_{OCP} = \pm 5$  mV over the course of the experiments with drift less than  $0.3$  mV  $\text{min}^{-1}$ , suggesting that the measurements did not induce major changes in the RE potential (see figure S5 in SI). The stability of the Ag/AgCl electrode, despite the occurrence of sizeable currents, is attributed to the presence of a sufficient number of chloride ions in the RE capillary (3 M KCl solution) as well as in the test solution (all buffers contain around 0.1 M KCl).

Further support that the observed Dirac point shift is indeed due to the current at the GLI is obtained by separating the graphene channel and the RE in two separate reservoirs, which were connected by a salt bridge [41]. A scheme of

the measurement setup is shown in figure 5(a). In the beginning, both reservoirs are filled with the blank buffer solution. Subsequently, the solution in either of the reservoirs is replaced with increasing concentrations of the redox probe and the field-effect is measured. Figures 5(b) and (c) present the observed changes when the redox probe is added only to the graphene reservoir and when it is added only to the RE reservoir, respectively. As summarized in figure 5(d) we see a shift in the Dirac point only for the case where  $[IrCl_6]^{2-}$  is added to the reservoir containing graphene. This result confirms that the interaction of the redox active species with the graphene itself is crucial for the shift to occur. Since no shift of the Dirac point is observed when the redox active molecule is added to the gate electrode reservoir, we conclude that the RE potential does not change due to varying concentrations of the redox probe, irrespective of where the RE is placed. This is expectedly indicative of a properly functioning RE. Furthermore, we found that the open circuit potential at the GLI does not correlate with shifts in the Dirac point in contrast to observations made on SWNTs, suggesting that the redox shift is non-Nernstian [47]. (See figure S6 and the associated discussion in the SI.)

In summary, putting all the above observations together brings us to the conclusion that the observed Dirac point shift is due to a change in the electrode potential of graphene because of the current due to heterogeneous ET. This indicates that the deployed graphene surface does not present a polarized interface [39]. Ideally for a liquid-gated FET one would like to have a polarized interface at graphene, where there are no interfacial currents in the range of the gate voltage interrogated. With the occurrence of a Faradaic current in the presence of a redox probe, there is a clear shift in the electrode potential, as reflected by the shifts in the Dirac point, and the interface deviates significantly from a polarized interface. Based

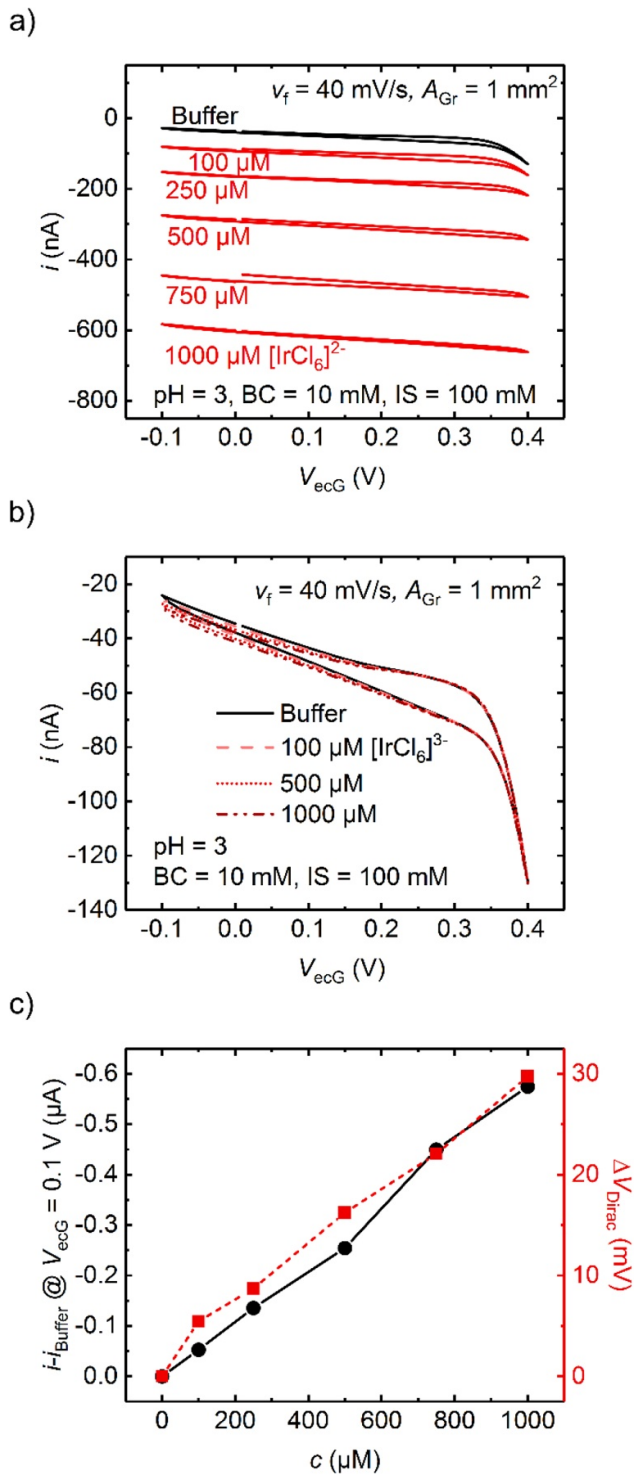


**Figure 3.** (a), (b) Two-electrode CVs for the device in figure 1 showing the current  $i$  between graphene and the RE as a function of  $V_{ecG}$  in the voltage range used for FET measurements. The currents in blank buffer (black curve) and in the presence of increasing concentrations of (a)  $[\text{IrCl}_6]^{2-}$  and (b)  $[\text{IrCl}_6]^{3-}$  are shown. The scan rate  $v_f$  is  $40 \text{ mV s}^{-1}$ , as was also the case for the FET measurements in figure 1. (c) Evolution of the Faradaic current component ( $i_c = i - i_{\text{Buffer}}$ ) at  $V_{ecG} = 0.1 \text{ V}$  as a function of the concentration of  $[\text{IrCl}_6]^{2-}$  (black cycles) and shift of the Dirac point for the same concentrations of  $[\text{IrCl}_6]^{2-}$  as shown in figure 1(d) (red squares).

on this model, the non-dynamic nature of the Dirac point shift (i.e. no variation with time) can also be explained. In the gate voltage range scanned, we are at a very cathodic potential for the  $[\text{IrCl}_6]^{2-}$  redox probe and, as a result, there is a rather constant diffusion-limited current, resulting in a constant polarization during the measurement time. This constant polarization results in a constant shift in the Dirac point for a given concentration of redox species.

### 2.3. Influence of electrode kinetics on the Faradaic effect

Now, we explore how one could modulate or minimize this Faradaic effect. From potentiodynamic measurements, it is known that the Faradaic current is diffusion-limited, a function of electrode area and dependent on the kinetics of ET [45]. With an increase in the electrode area, the magnitude of the Faradaic current is expected to increase. In contrast, electrostatic interactions and charge transfer doping effects modulate charge carrier *density* in the transistor channel and the resulting threshold voltage shifts are typically independent of the size of the electrode. This difference motivates the investigation of the observed responses as a function of the electrode area. To obtain a quantitative dependence of the observed shift as a function of the electrode area, it is necessary to have the capability to vary the size of the graphene sheet (which forms the FET channel) continuously. With this goal, we have realized a new setup, schematically shown in figure 6(a). Graphene devices prepared with a specialized layout, as shown in figure 6(b), are used for this purpose. The contacted graphene device is mounted on a micrometer Z-stage, and the sample can be gradually lowered (in  $50 \mu\text{m}$  steps) into a liquid solution equipped with a Ag/AgCl RE. At every dipping step, the gate dependence of conductance or the field-effect can be measured. In this manner, the area of the gated FET channel can be dynamically varied and is directly proportional to the depth up to which the sample is immersed. Figure 6(c) presents a map showing the evolution of the field-effect in blank buffer as the area of the graphene flake increases. (Selected individual gate scan cycles are shown in figure S7 in the SI). From the Dirac point values overlaid in white on this image, it is apparent that the Dirac point shows minimal shifts as a function of the electrode size. Figure 6(d) presents the same map measured in a solution of the oxidized species  $[\text{IrCl}_6]^{2-}$ . With increasing area, the Dirac point is found to shift further away from the value in blank buffer. Figure 6(e) summarizes the evolution of the Dirac point for these two cases along with the behavior for the reduced form  $[\text{IrCl}_6]^{3-}$ , where it can be seen that the area-dependent response is observed only for  $[\text{IrCl}_6]^{2-}$  and that  $\Delta V_{\text{Dirac}}$  is roughly linearly proportional to the electrode area. The same set of measurements was carried out in blank buffers of three different pH [6], shown in figure 6(f). For this case, the position of  $V_{\text{Dirac}}$  presents a similar offset as a function of pH for all electrode sizes. As mentioned earlier, the pH of the solution sets the surface charge density at the GLI, and hence the Dirac point value is not dependent on the area of the FET channel. These data clearly differentiate the shift due to redox

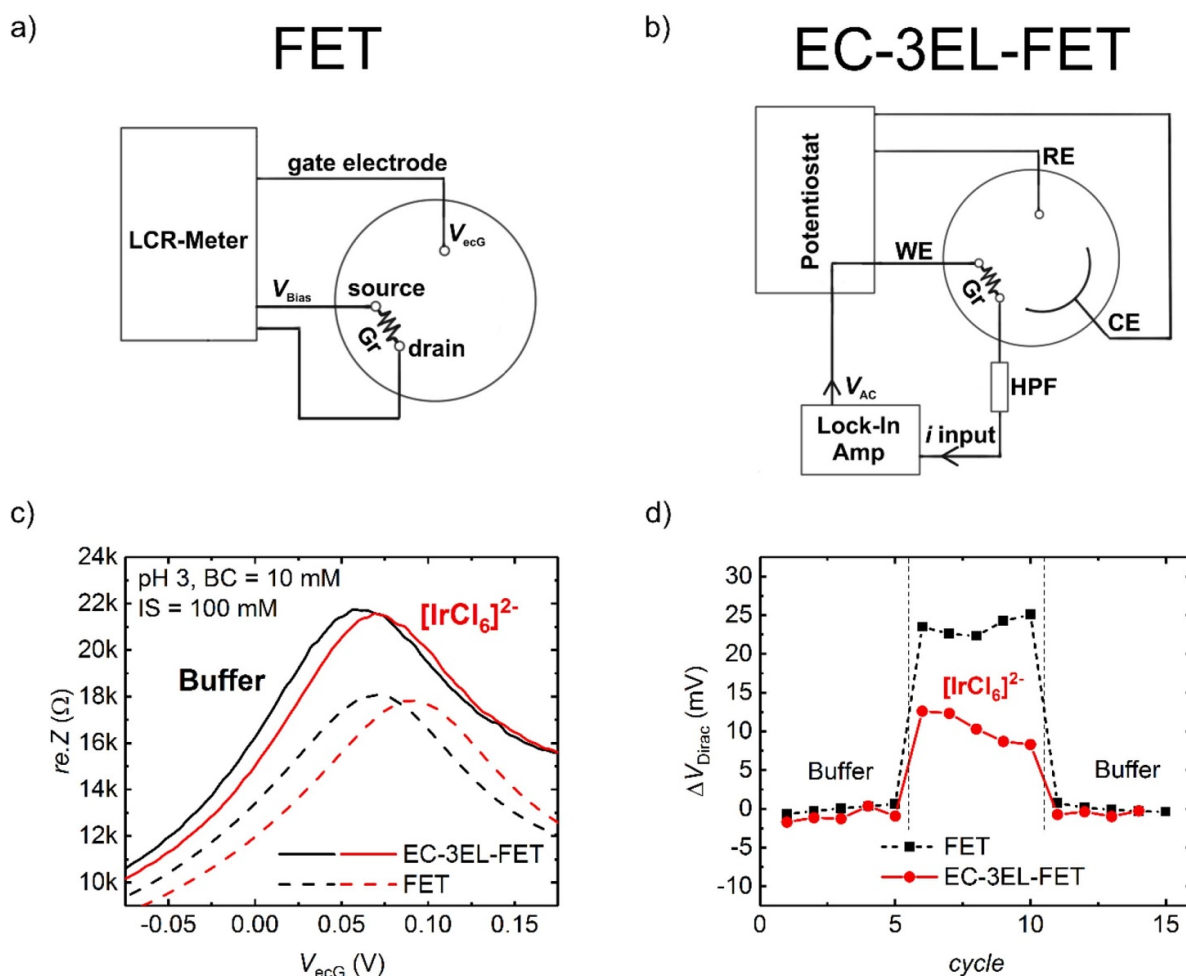


**Figure 4.** Field-effect measurements with three-electrode potentiostatic control (EC-3EL-FET). Circuit diagrams of (a) the commonly used two-electrode FET setup and (b) of the EC-3EL-FET setup, which allows for the parallel measurement of electrochemical currents and the conductance of the graphene electrode as a function of the applied RE potential/gate voltage. Gr: graphene, HPF: high pass filter. (c) A comparison of shift introduced by [IrCl<sub>6</sub>]<sup>2-</sup> (1 mM) in standard FET (dashed lines) and EC-3EL-FET (straight lines). (d) The position of the Dirac point for multiple cycles of the measurements (black squares: FET, red circles: EC-3EL-FET). For better comparability, the position of  $V_{\text{Dirac}}$  is normalized to the average position of  $V_{\text{Dirac}}$  in blank buffer. (See figure S8 for area-dependent measurements.)

active species from doping due to electrostatic effects, and is in line with the explanation presented earlier. Measurements with potentiostatic control (three-electrode setup, avoiding any polarization of the RE) also show a Dirac point shift proportional to the electrode area for the [IrCl<sub>6</sub>]<sup>2-</sup> (see figure S8 in the SI). Please note that we have focused here only on the two-electrode configuration, since this is the common configuration used in most of the electrochemically gated measurements in the literature.

Since a redox Faradaic current induces the Dirac point shift, it is expected that there should be some correlation between the shift and the kinetics of ET. We show that this is indeed the case by considering the interaction of an inner sphere redox probe [Fe(CN)<sub>6</sub>]<sup>3-/4-</sup> with graphene [7, 21–23, 25, 43, 48]. Figure 7(a) presents Dirac point shifts observed for increasing concentrations of the reduced and oxidized forms. The complete measurements are shown in figure S9 in the SI. The formal potential of this redox probe on the  $V_{\text{ecG}}$  scale is  $-0.22\text{ V}$  ( $E^0 = +0.22\text{ V}$  vs Ag/AgCl), which is again in the valence band of graphene. Hence, the Dirac point shifts to

more positive voltages in the presence of the oxidized form [Fe(CN)<sub>6</sub>]<sup>3-</sup> (analogous to the case of [IrCl<sub>6</sub>]<sup>2-</sup>) and a cathodic/reductive current was observed, which is discussed in figure S10 in the SI. A small shift is also observed for the reduced species [Fe(CN)<sub>6</sub>]<sup>4-</sup>. This can be understood by considering that in the scanned potential range ( $V_{\text{ecG}} = -0.1\text{ V}$  to  $+0.4\text{ V}$ ) it is very likely that a small proportion of [Fe(CN)<sub>6</sub>]<sup>4-</sup> is oxidized and re-reduced, which is the reason for the observed minimal shifts. (See figure S11 in the SI for a more detailed discussion of this phenomenon.)

Typically, the kinetics of electrode reactions can be affected by varying the applied potential ( $E_{\text{appl}}$  or equivalently  $V_{\text{ecG}}$ ) [45]. However, we modulate  $V_{\text{ecG}}$  to measure the field-effect itself. Hence, it is not possible to decouple the electrode kinetics completely when performing a field-effect measurement in liquids. An alternative way to modulate electrode kinetics is to vary the solution conditions, such as pH. We recently demonstrated that a variation in pH leads to a modulation of ET rates at graphene monolayer electrodes [21]. Specifically, anions such as [Fe(CN)<sub>6</sub>]<sup>3-/4-</sup> are found to exhibit

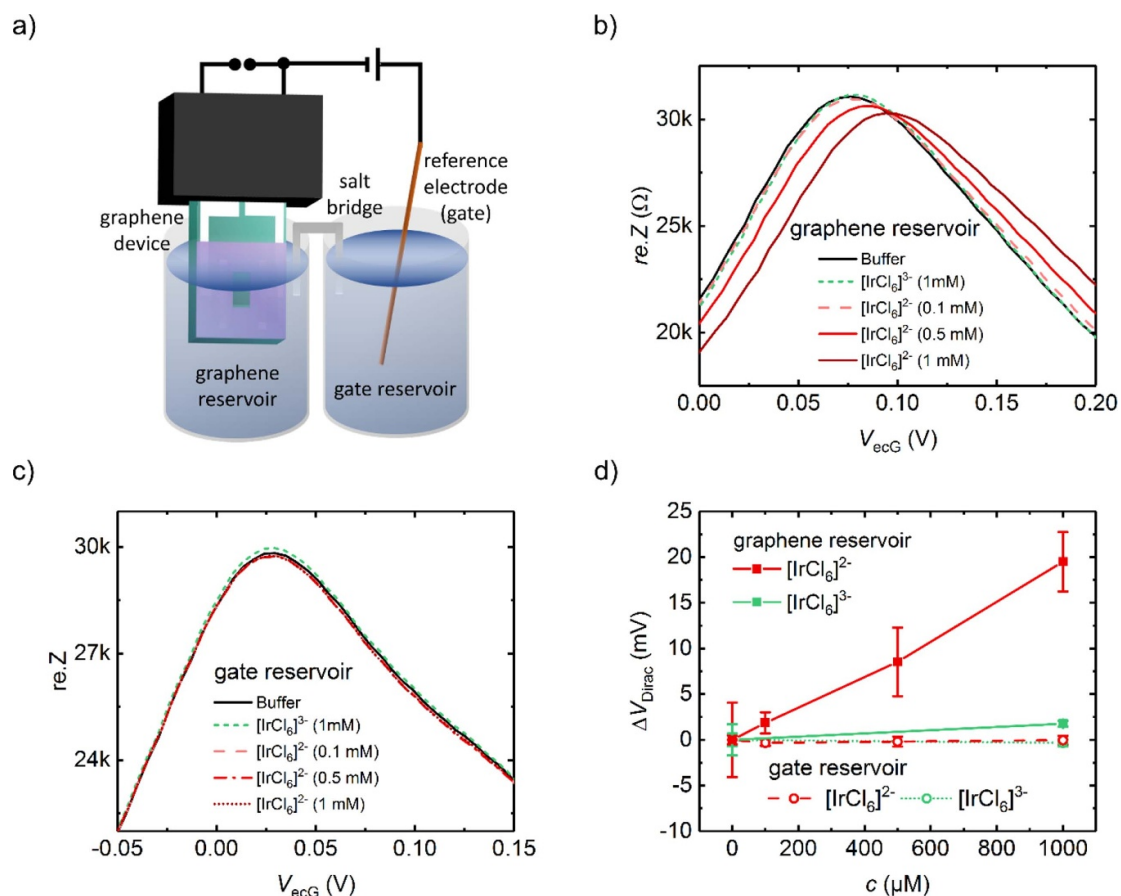


**Figure 5.** (a) A schematic showing the setup for field-effect measurements with the RE (gate) placed in a separate reservoir and connected to the graphene device reservoir through a salt bridge. (b), (c) Gate dependence of the resistance of a graphene device with varying concentrations of the redox probes  $[\text{IrCl}_6]^{2-}$  (red) and  $[\text{IrCl}_6]^{3-}$  (green). In (b) the redox probes were only added to the graphene reservoir and the gate reservoir contained blank buffer (pH 3, BC = 10 mM, IS = 100 mM). In (c) the redox probes were only added to the gate reservoir and the graphene reservoir contained blank buffer. (d) A plot of  $\Delta V_{\text{Dirac}}$  as a function of the concentration of  $[\text{IrCl}_6]^{2-}$  or  $[\text{IrCl}_6]^{3-}$  extracted from (b) and (c).

significantly lower ET rates at high pH, mainly attributed to electrostatic interactions between ionizable groups at the GLI and the charge of the redox probe. Figure 7(b) compares Dirac point shifts observed for varying concentrations of the oxidized species  $[\text{Fe}(\text{CN})_6]^{3-}$  in three different solutions of varying pH. It is apparent that the slopes of the curves are significantly lower at high pH. At this pH, the ET rates are about an order of magnitude lower in comparison to the rates at low pH [21] and, as a result, the observed Dirac point shifts are much weaker. Finally, it can be shown that the magnitude of the observed shifts are affected by the diffusion of the redox active species to the electrode surface. Figure 7(c) presents the dependence of the observed shifts against the square root of the scan rate, where the classical scan rate dependence for the electrochemical current at a planar electrode [45] is apparent. This behavior is also unlike what is typically observed for electrostatic or charge transfer doping effects. These kinetic effects can be observed for the outer-sphere redox couple  $[\text{IrCl}_6]^{2-}$  as well. But the pH-effect is more pronounced for  $[\text{Fe}(\text{CN})_6]^{3-}$ . Additionally, the effect of scan direction on the observed Dirac point shift is discussed in figure S12 in the SI for both redox probes.

#### 2.4. General characteristics of the Faradaic effect

It is worth mentioning that when considering kinetic effects we can mainly compare the data measured with one redox probe. The ET rates are quite different for  $[\text{Fe}(\text{CN})_6]^{3-/4-}$  and  $[\text{IrCl}_6]^{2-/3-}$  [21]. Additionally, one should be cautious when comparing the magnitude of threshold voltage shifts for these two cases directly. This is because the Faradaic current at the GLI will be dictated by the exchange current density for a given redox species, and this may be quite different for these two cases as well. Furthermore, the scanned gate potential with respect to  $E^0'$  will determine the operating overpotential, which will be different from one redox couple to the other. Nevertheless, we can already make several generalizations regarding this unique Faradaic effect. Firstly, it is clear that the effect is dictated by electrode area and hence can be modulated depending on the application of interest. Figure 8 presents shifts in  $V_{\text{Dirac}}$  measured at a graphene device of comparably small area ( $40 \times 40 \mu\text{m}^2$ ) along with the profile for the large-area graphene device ( $1.1 \text{ mm}^2$ ). Here, it is apparent that the shift in  $V_{\text{Dirac}}$  as a function of the concentration of  $[\text{IrCl}_6]^{2-}$  is rather minimal for the small-area device. This can be understood by considering that at small-area electrodes

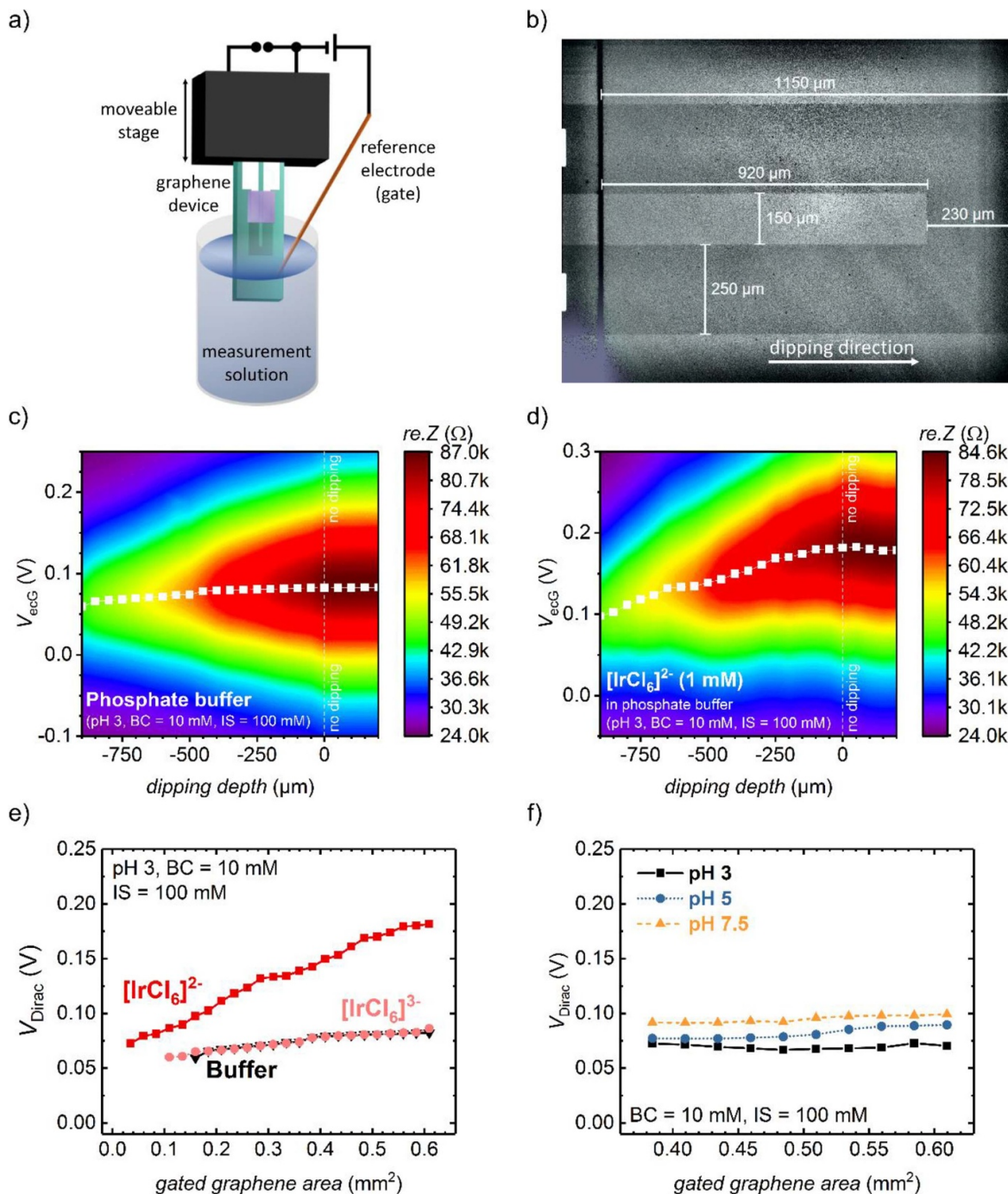


**Figure 6.** Area dependence of the field-effect in graphene. (a) A schematic of the experimental setup showing the device mounted on a motorized Z-stage, with the help of which the device can be gradually dipped into a test solution. With every dipping step, the gated area of the graphene FET channel is increased in well-defined steps. (b) An optical image of a graphene device with the U-shaped channel for dipping experiments. (c), (d) Evolution of the gate dependence of resistance (*re.Z*) with increasing dipping depth in (c) blank buffer and with (d) 1 mM  $[\text{IrCl}_6]^{2-}$ . After reaching the maximum dipping depth, the measurement was continued for some cycles to show the stable response at a constant dipping depth (marked by the dashed line at 0  $\mu\text{m}$  and the indicator ‘no dipping’). Refer to section 4 for details of this measurement. The white profile corresponds to the Dirac point in every cycle. (e) A plot of  $V_{\text{Dirac}}$  as a function of graphene area in blank buffer solution and in the presence of oxidized  $[\text{IrCl}_6]^{2-}$  or reduced  $[\text{IrCl}_6]^{3-}$ , each at a concentration of 1 mM. (f) A plot of  $V_{\text{Dirac}}$  as a function of graphene area in blank buffer solutions of varying pH (BC = 10 mM, IS = 100 mM). The plots in (e) and (f) are extracted from maps such as in (c) and (d).

( $\mu\text{m}^2$  range), the Faradaic current is in the low nA regime (see figure S13 in the SI). As a result, there is little polarization at the GLI and the contribution of this effect to the effectively

observed shift in the Dirac point is rather low and can be virtually neglected. However, the purpose of this work was to investigate the effect of electrochemical currents in field-effect

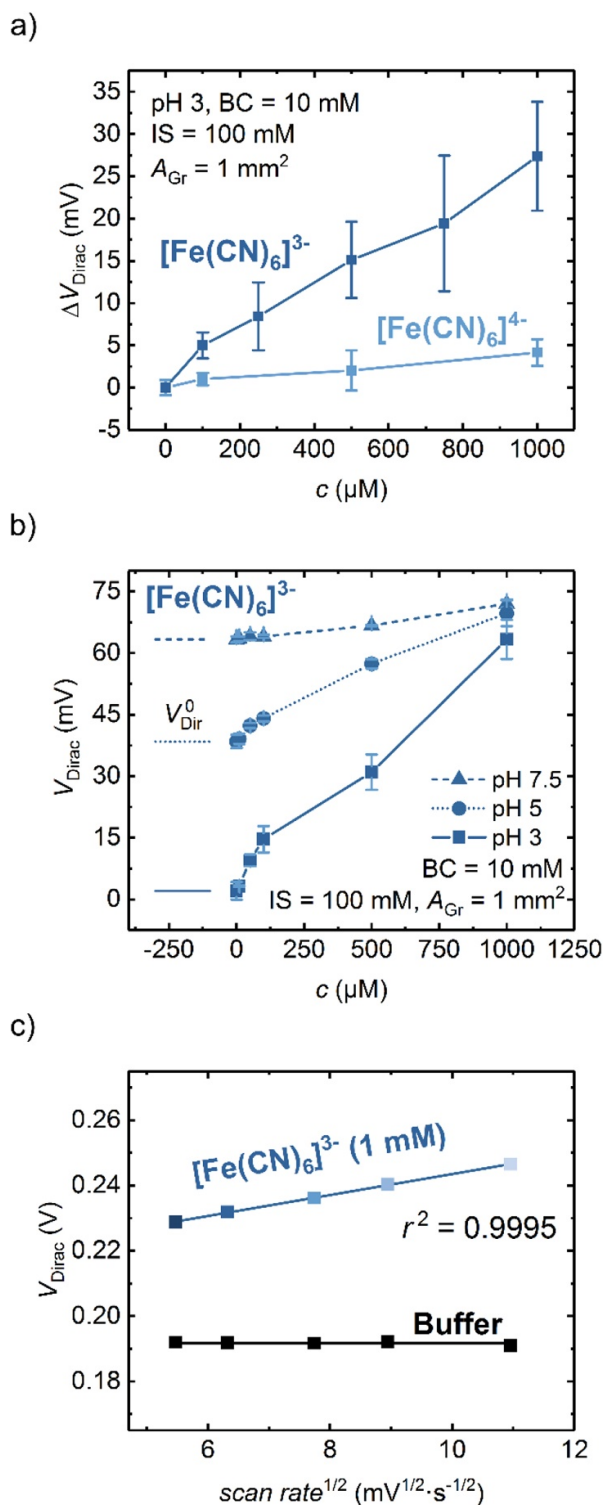


**Figure 7.** The Faradaic effect with the  $[\text{Fe}(\text{CN})_6]^{3-/4-}$  redox probe. (a) Evolution of the shift in Dirac point  $\Delta V_{\text{Dirac}}$  (with respect to the Dirac point in blank buffer) as a function of the concentration of oxidized  $[\text{Fe}(\text{CN})_6]^{3-}$  and reduced  $[\text{Fe}(\text{CN})_6]^{4-}$ . The complete dataset is shown in figure S9 in the SI. (b) Concentration dependent shift in the Dirac point of another graphene device as a function of the concentration of  $[\text{Fe}(\text{CN})_6]^{3-}$  in buffer solutions of varying pH at fixed buffer concentration (BC) and IS. The position of  $V_{\text{Dirac}}^0$  (Dirac point in blank buffer) shifts as a function of the pH, as indicated in the graph. (c)  $V_{\text{Dirac}}$  as a function of the square root of the scan rate along with a linear fit in the presence of  $[\text{Fe}(\text{CN})_6]^{3-}$  (1 mM) and in blank buffer.

measurements. Hence, the graphene area was chosen to be big enough for Faradaic currents to be significant. In contrast to this area-dependent Faradaic effect, electrostatic effects are independent of electrode size. To demonstrate this, we have measured the pH and ionic strength (IS) sensitivity of both types of devices [6]. As shown in figure 8(b), irrespective of the graphene area, the shift of the Dirac point in solutions of varying pH and IS can be detected with similar sensitivity, which is a characteristic of the electrostatic nature of the interfacial interactions in this case.

Secondly, the Faradaic effect is linearly proportional to the concentration, and hence small amounts of redox species will have a significantly lower effect on the observed shifts. Thirdly, electrode reactions with a low exchange current density will not introduce a significant shift. Finally, the most important aspect is that the kinetics of ET will dictate the strength of the observed Faradaic effect. The last two aspects are interesting, since both the exchange current density and the ET kinetics can be improved by catalysts at the electrode surface, introduced deliberately or present as trace impurities after the transfer [44]. In both cases, a much stronger Faradaic effect may be observed. In applications, where detection of charge is the main goal, the Faradaic effect may be a parasitic effect [39]. Based on the results presented here, it is quite clear that this effect can be minimized rather completely by the suggestions mentioned above. Another approach is to engineer the design of the GLI to ensure low ET rates in graphene. By introducing functional layers (non-covalently) on top of graphene, the direct interaction of graphene with redox active species may be restricted, the ET rates reduced and Faradaic effects suppressed, while the GLI becomes increasingly polarized. Indeed, this approach has been used in many biosensors based on nanostructures reported until now [9, 49, 50]. The attachment of functional layers may also be done covalently, which also leads to a reduction in ET rates [51, 52]. A disadvantage with this approach is, however, that the mobility of charge carriers in graphene may be reduced [53–55].

### 2.5. Implications of the Faradaic effect for sensor design

Now we turn towards a discussion of the consequence of this Faradaic effect in graphene field-effect sensors. For large-area graphene devices, the GLI is not perfectly polarized and measures are required to suppress the Faradaic currents at the interface to get closer to realizing an ideal polarized interface, which is necessary for field-effect sensing [39]. This control is of utmost importance for all GFET applications, especially since a huge variety of biologically relevant molecules are, in fact, electrochemically active. Examples range from molecules like methylene blue [56] or nicotinamide adenine dinucleotide dehydrogenase (NADH) [24, 57], through enzymes or their cofactors, such as glucose oxidase and flavin adenine dinucleotide (FAD) [58–60], to electrochemically active bacteria [61]. Our results for the canonical redox couples  $[\text{IrCl}_6]^{2-/3-}$  and  $[\text{Fe}(\text{CN})_6]^{3-/4-}$ , which we employed as model systems, clearly show that electrochemical activity that leads to Faradaic currents in the measurement window of the gate modulation of graphene affects the

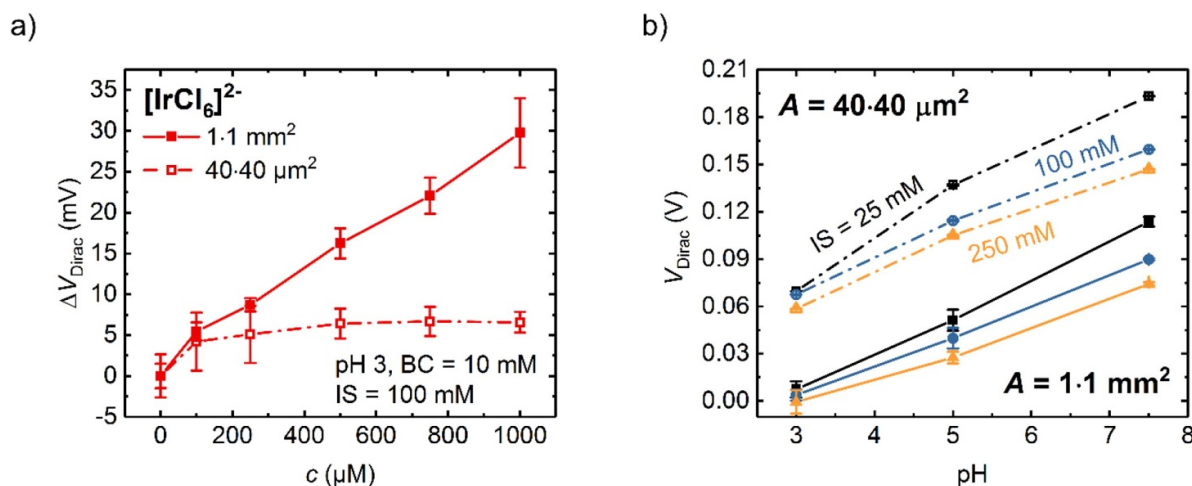


**Figure 8.** Comparison of the sensitivity of graphene devices with large and small graphene areas. (a) The  $\Delta V_{\text{Dirac}}$  as a function of probe concentration  $[\text{IrCl}_6]^{2-}$  for graphene devices of two different electrode areas:  $1.1 \text{ mm}^2$  and  $40 \cdot 40 \mu\text{m}^2$ . (b) The pH- and IS-dependent position of  $V_{\text{Dirac}}$  in buffers at pH 3, 5 and 7.5 and IS of 25, 100 and 250 mM on samples with a graphene area of  $1.1 \text{ mm}^2$  and  $40 \cdot 40 \mu\text{m}^2$ . For details of buffer composition, see table S1 in the SI. The IS is adjusted by the addition of appropriate amounts of KCl.

stability of the Dirac point. If redox active molecules, however, are used as receptors or targeted as analytes in electrochemically gated GFET sensors, this electrochemical activity will be detrimental to the sensor response. The same may apply for molecules deposited on top of graphene as anchor layers, like polyaniline- or polypyrrole-derivatives, which occupy varying oxidation states based on the solution pH when undergoing electrochemical rearrangement reactions [9, 62, 63]. On large-area graphene devices, these reactions could result in large currents leading to a Faradaic effect. This problem can be overcome by using small-area graphene devices.

A key finding of this work is that in small-area graphene devices showing ultramicroelectrode behavior, redox probes introduce only minimal changes in the field-effect characteristics. This is contrary to the case of back-gated and non-gated graphene devices, where charge transfer has been proposed as a viable mechanism for explaining the sensor response [18, 40]. Although charge transfer does occur with graphene in electrochemically gated GFET sensors, as evidenced by the electrochemical Faradaic steady state currents, this is not accessible using field-effect measurements in liquid with electrochemical gating, as we have outlined in detail here. On the other hand, this insensitivity to redox active species is an advantage for small-area electrochemically gated graphene sensors, since they are mainly sensitive to interfacial electrostatic potential, as would be required for a polarized electrode in an FET configuration [39]. As changes in the electrostatic charge distribution are typically behind the sensing mechanism of biomolecules [2, 4, 9–15, 64], the Faradaic effect should be avoided, e.g. by using micro-structured graphene. For the detection of analytes that undergo only charge transfer, an electrochemical analysis (e.g. voltammetry) appears to be more sensitive and better suited than field-effect measurements. On the other hand, facilitating the Faradaic effect as a transduction mechanism in studies based on electrochemically gated large-area GFETs might open a route for new sensor

designs. In fact, the Faradaic effect appears to be behind the sensor response of a glucose sensor, where glucose oxidase was electrochemically re-oxidized at graphene leading to a Dirac point shift similar to the Faradaic effect described here [65].

Now, one wonders if such an effect may also occur in other 2D materials. Based on our results it can be said that this will depend a lot on the electronic structure of the 2D material. Many other materials such as  $\text{MoS}_2$  are semiconductors, and hence the Faradaic effect will depend very much on the potential range used in field-effect measurements and the standard potential of the redox species. In large-area FET devices based on 2D materials similar effects may be expected when the potential range is well within the conduction or valence band. Future work with these materials may shed further light on this aspect.

### 3. Conclusion

In conclusion, we have investigated the interaction of redox active molecules with graphene in detail and found that ET to these probes causes shifts in the Dirac point, which is termed a Faradaic effect in electrochemically gated graphene FETs. The presented results show that this kind of shift is observed only under certain conditions. Oxidized species cause a shift only if the formal potential lies in the valence band. The investigation of the effect of reduced species with the formal potential in the conduction band is a goal for future work. The magnitude of the shift is found to be linearly proportional to the concentration of the redox probe and electrode area, which correlates well with the nature of Faradaic currents observed in electrochemical processes. Moreover, the Faradaic effect is dictated by the kinetics of the electrode reaction, which differentiates this effect clearly from electrostatic or charge transfer doping transduction mechanisms. Furthermore, in contrast to these

latter effects, which require binding of the species to the surface, the Faradaic effect does not require binding of molecules to the surface. Finally, we have discussed that redox active probes do not induce changes in field-effect characteristics when the graphene FET channel area is small. The same may be expected if the kinetics are hampered by covalent or non-covalent functionalization. In these cases, the GLI approaches an ideal polarized interface. Our results have important implications for the field of electrochemically gated graphene FET sensing devices, as we demonstrate a new sensing mechanism, which needs to be considered in sensor design. For electrochemically active (bio)molecules, this Faradaic effect can be parasitic in sensing. Therefore, the occurrence of Faradaic currents due to electrochemical activity of the molecules used to design a specific biosensor and/or the targeted analytes should always be monitored and minimized in electrical sensors operating in liquid, especially if graphene is used as the transducer.

## 4. Experimental

### 4.1. Device fabrication

A list of the used chemicals can be found in the SI. Graphene (CVD-grown monolayer graphene on copper foil) was purchased from Graphenea. Graphene devices were fabricated on silicon (100) wafers (500 nm SiO<sub>2</sub> wet-oxide, *n*-type, dopant: antimony, 0.005–0.025 Ω cm, Siltron Inc., Korea). A scheme visualizing the process flow of fabrication steps can be found in figure S1 in the SI. The electrode layout, graphene patterning and electrode passivation were accomplished by photolithography, for which a HIMT MLA100 maskless aligner was used ( $\lambda_{\text{exc}}$ : 365 nm). For the electrode layout (figure S1(a) in the SI), the sample was covered with positive photoresist S1805 by spin-coating, dried (2:20 min at 95 °C) and exposed (90 mJ). The layout was developed in mf-319 developer (30 s with agitation), rinsed with water and blow-dried using a pressurized air stream. Subsequently, 50 nm Ti and 10 nm Pt were evaporated. The lift-off of the photoresist was carried out in *N*-ethylpyrrolidone (NEP, twice, at 55 °C), followed by agitation in acetone and isopropanol. Immediately prior to the transfer of graphene, the samples were cleaned again in NEP, acetone and isopropanol for 10 min each in the ultrasound bath, followed by a Piranha treatment (H<sub>2</sub>SO<sub>4</sub>/H<sub>2</sub>O<sub>2</sub>, 6:1) for 30 s. For transfer (figure S1(b) in the SI), graphene was covered with polystyrene (PS) by drop casting a solution of PS in toluene and drying for 10 min each at room temperature (RT) and at 75 °C. Copper was then removed in etching solution (H<sub>2</sub>O<sub>2</sub>/HCl/H<sub>2</sub>O 1:3:16). The PS-protected graphene was washed with H<sub>2</sub>O, dilute HCl (100 mM) and again with H<sub>2</sub>O before it was scooped out. Then, the sample was dried at RT, 75 °C and 95 °C for 10 min each. The PS was removed in toluene (5 min with agitation). The devices were then annealed at 600 °C in N<sub>2</sub> atmosphere for 2 min to enhance the adhesion of graphene to the Si/SiO<sub>2</sub> surface. A desired graphene layout was patterned using the photoresist S1805 as displayed in figure S1(c) in the SI. The uncovered graphene was removed using oxygen plasma (0.5 mbar, 2 min). After that, the photoresist was removed by lift-off in NEP (twice),

acetone and isopropanol for 30 s each. Finally, the metal contacts were passivated using the negative photoresist SU-8 10 (figure S1(d) in the SI). The photoresist was spin coated, dried (2 min at 65 °C, 5 min at 95 °C), and exposed (300 mJ). After post-baking (1 min at 65 °C, 2 min at 95 °C), the resist was developed in mrDev600 for 55 s with agitation, washed with isopropanol and blow-dried. Three different layouts were used. The standard device has two electrode contacts with a gap of 1200 μm and a width of 1000 μm. The graphene is patterned with a width of 1000 μm, covering both electrodes and the gap in between. The passivation covers the electrodes and 100 μm of graphene at the contacts. Thereby, a graphene area of 1 × 1 mm<sup>2</sup> is fabricated as the conductive channel of the GFET. The small-area samples were fabricated in a similar manner with a final sheet size of 40 × 40 μm<sup>2</sup>. For the measurement of area dependence, the graphene is patterned in a U-shape. The dimensions of this shape are depicted in the optical image of figure 6(b).

### 4.2. Graphene characterization

Graphene samples have been characterized using atomic force microscopy (AFM) and Raman spectroscopy to ensure the graphene was clean and in mostly defect-free condition after the sample fabrication. AFM images were obtained using a NanoScope Dimension 3100 in tapping mode. Raman spectra were recorded with a JASCO NRS-4100 Raman spectrometer equipped with a 1650-256 CCD detector (Andor; air/Peltier-cooled to –60 °C) with a 400 Lines/mm grating. A diode laser with an excitation wavelength of 632.8 nm (13.6 mW laser power) and a 100× (NA 0.90) objective were used for the measurements. See figure S2 in the SI for AFM and Raman characterization of a typical device.

### 4.3. Field-effect and electrochemical measurements

For FET measurements, an Agilent E4980A Precision LCR meter was used. The impedance of the graphene device was measured with an AC voltage of 10 mV applied between the two contacts at a frequency of 1027 Hz. The real part of the impedance *re.Z*, which corresponds to the resistance (phase approaches 0°), is recorded as a function of the gate voltage. A polydimethylsiloxane (PDMS) channel was placed on top of the device and a droplet of solution (70–150 μl) was applied. A Ag/AgCl (3 M KCl) capillary RE was used as the gate. Before any device was used for measurements, the graphene surface was cleaned of trace metal impurities by cycling the gate voltage (+0.6 to –0.3 V) in HCl (100 mM) [44], until the position of the Dirac point was stable. The field-effect response was recorded in every buffer for 3–5 cycles and the average was calculated neglecting the first cycle. The error bars in the graph show the maximum deviation of the Dirac point from all cycles around this mean value. Subsequently, the scan is paused close to a gate voltage of 0 V, and the solution is exchanged by removal of approx. 2/3 of the solution and application of the next solution. This is repeated at least ten times (more often for more concentrated samples). At the beginning and at the end of a measurement series, the

field-effect is recorded in the same blank buffer, to determine any drifts introduced during the series. If constant drifts are present, they are subtracted during analysis. For the scan rate dependent measurement, the buffer solution was applied and the gate voltage window was scanned three times at each scan rate. Subsequently, the solution containing the redox active species was applied and the same measurements were performed. Finally, the experiment was repeated in blank buffer solution. Only the position of the Dirac point during the forward sweep of the third cycle of each measurement was used for evaluation to allow the system to reach a steady state. For electrochemical experiments, the same device setup with the PDMS well was used. For three-electrode electrochemical measurements, an additional platinum wire electrode was placed in the solution as the counter electrode. Both graphene contacts were used as the WE, to ensure that the whole graphene channel was contacted. The same RE (WPI Dri-Ref-450 Reference Electrode) was used for CVs as for GFET measurements. The buffer compositions are given in table S1 in the SI. For field-effect measurements with potentiostatic control in a three-electrode cell (graphene WE, Pt counter electrode and Ag/AgCl RE), a lock-in amplifier (Ametek SR7265) was used to apply an AC bias to the graphene WE. The AC current through graphene was picked up through the other contact by the current input of the lock-in amplifier after passing a high pass filter and the resistance extracted from the measured current. The voltage was chosen to have the same parameters as the impedance measurements (10 mV at 1027 Hz). A circuit diagram of this setup is shown in figure 4. Measurements comparing common two-electrode FET measurements and three-electrode FET measurements with potentiostatic control were performed in 10 ml beakers.

#### 4.4. Area dependence of field-effect response

For the measurements in figure 6, a forward and backward scan are recorded at every dipping depth. At the end of the backward scan, the sample is moved 50  $\mu\text{m}$  deeper into the solution. As soon as graphene is in touch with the solution, the Dirac point is observable. However, the actual area-dependence is observable only after the bottom of the U-shaped graphene is passed. In this area-realm, the area-dependent measurement is hindered by graphene's hydrophobic character: Only after several dipping steps, the solution will surpass the lower graphene edge, wetting graphene reliably. For the same reason, the backward scan is used for evaluation of the Dirac point. We refer to the dipping depth as seen from the upper edge of graphene (at the passivation, with 0  $\mu\text{m}$  at this point) in negative steps of 50  $\mu\text{m}$  down to the lower edge at  $-1150 \mu\text{m}$ . Hence, the most relevant part is found from the 6th step ( $-900 \mu\text{m}$ ) up until the whole channel is dipped into the solution. Each step in this realm is equivalent to a change of  $0.025 \text{ mm}^2$  ( $25\,000 \mu\text{m}^2$ ). For each sample, the response in blank buffer is recorded first, followed by the test solution and finally the blank buffer again, to ensure that the initial response could be reproduced. The channel consists of an assembly of graphene domains, which may have variable Dirac point values due to differences in doping. Hence, a slight variation of the Dirac point over depth is

possible, even if no interacting species is present in the analyte solution.

## Acknowledgments

We thank Stephan Schmid and Birgit Lemke from MPI Stuttgart for help with metal deposition, as well as Martin Muske from HZB and Michael Winterfeld from HU Berlin for help with sample preparation.

## Funding

Funding from the German Science Foundation (DFG) as part of the excellence initiative via the Graduate School of Analytical Sciences Adlershof (GSC1013 SALSA) is gratefully acknowledged.

## Conflict of interest

The authors declare no conflict of interest.

## ORCID iDs

Tilmann J Neubert  <https://orcid.org/0000-0002-0049-4536>

Michel Wehrhold  <https://orcid.org/0000-0002-9633-5547>

Kannan Balasubramanian  <https://orcid.org/0000-0003-2663-7790>

## References

- [1] Stine R, Mulvaney S P, Robinson J T, Tamanaha C R and Sheehan P E 2013 Fabrication, optimization, and use of graphene field effect sensors *Anal. Chem.* **85** 509–21
- [2] Balasubramanian K and Kern K 2014 25th anniversary article: label-free electrical biodetection using carbon nanostructures *Adv. Mater.* **26** 1154–75
- [3] Reina G, Gonzalez-Dominguez J M, Criado A, Vazquez E, Bianco A and Prato M 2017 Promises, facts and challenges for graphene in biomedical applications *Chem. Soc. Rev.* **46** 4400–16
- [4] Fu W, Jiang L, van Geest E P, Lima L M C and Schneider G F 2017 Sensing at the surface of graphene field-effect transistors *Adv. Mater.* **29** 1603610
- [5] Heller I, Kong J, Williams K A, Dekker C and Lemay S G 2006 Electrochemistry at single-walled carbon nanotubes: the role of band structure and quantum capacitance *J. Am. Chem. Soc.* **128** 7353–9
- [6] Zuccaro L, Krieg J, Desideri A, Kern K and Balasubramanian K 2015 Tuning the isoelectric point of graphene by electrochemical functionalization *Sci. Rep.* **5** srep11794
- [7] Brownson D A, Kampouris D K and Banks C E 2012 Graphene electrochemistry: fundamental concepts through to prominent applications *Chem. Soc. Rev.* **41** 6944–76
- [8] Macedo L J A, Iost R M, Hassan A, Balasubramanian K and Crespilho F N 2019 Bioelectronics and interfaces using monolayer graphene *ChemElectroChem* **6** 31–59
- [9] Zuccaro L, Tesaro C, Kurkina T, Fiorani P, Yu H K, Knudsen B R, Kern K, Desideri A and Balasubramanian K 2015 Real-time label-free direct electronic monitoring of

- topoisomerase enzyme binding kinetics on graphene *ACS Nano* **9** 11166–76
- [10] Okamoto S, Ohno Y, Maehashi K, Inoue K and Matsumoto K 2012 Immunosensors based on graphene field-effect transistors fabricated using antigen-binding fragment *Jpn. J. Appl. Phys.* **51** 06FD08
- [11] Fu W, Feng L, Panaitov G, Kireev D, Mayer D, Offenhäusser A and Krause H-J 2017 Biosensing near the neutrality point of graphene *Sci. Adv.* **3** e1701247
- [12] Xu S *et al* 2017 Real-time reliable determination of binding kinetics of DNA hybridization using a multi-channel graphene biosensor *Nat. Commun.* **8** 14902
- [13] Cai B, Wang S, Huang L, Ning Y, Zhang Z and Zhang G-J 2014 Ultrasensitive label-free detection of PNA–DNA hybridization by reduced graphene oxide field-effect transistor biosensor *ACS Nano* **8** 2632–8
- [14] Ohno Y, Maehashi K, Yamashiro Y and Matsumoto K 2009 Electrolyte-gated graphene field-effect transistors for detecting pH and protein adsorption *Nano Lett.* **9** 3318–22
- [15] Blaschke B M, Lottner M, Drieschner S, Calia A B, Stoiber K, Rousseau L, Lissourges G and Garrido J A 2016 Flexible graphene transistors for recording cell action potentials *2D Mater.* **3** 025007
- [16] Fu W, Nef C, Knopfmacher O, Tarasov A, Weiss M, Calame M and Schönenberger C 2011 Graphene transistors are insensitive to pH changes in solution *Nano Lett.* **11** 3597–600
- [17] Aguirre C M, Levesque P L, Paillet M, Lapointe F, St-Antoine B C, Desjardins P and Martel R 2009 The role of the oxygen/water redox couple in suppressing electron conduction in field-effect transistors *Adv. Mater.* **21** 3087–91
- [18] Levesque P L, Sabri S S, Aguirre C M, Guillemette J, Siau M, Desjardins P, Szkopek T and Martel R 2011 Probing charge transfer at surfaces using graphene transistors *Nano Lett.* **11** 132–7
- [19] Kulkarni G S, Zang W and Zhong Z 2016 Nanoelectronic heterodyne sensor: a new electronic sensing paradigm *Acc. Chem. Res.* **49** 2578–86
- [20] Traversi F, Raillon C, Benameur S M, Liu K, Khlybov S, Tosun M, Krasnozhan D, Kis A and Radenovic A 2013 Detecting the translocation of DNA through a nanopore using graphene nanoribbons *Nat. Nanotechnol.* **8** 939
- [21] Wehrhold M, Neubert T J, Yadav A, Vondráček M, Iost R M, Honolka J and Balasubramanian K 2019 pH sensitivity of interfacial electron transfer at a supported graphene monolayer *Nanoscale* **11** 14742–56
- [22] Ritzert N L, Rodríguez-López J, Tan C and Abruña H D 2013 Kinetics of interfacial electron transfer at single-layer graphene electrodes in aqueous and nonaqueous solutions *Langmuir* **29** 1683–94
- [23] Velický M *et al* 2014 Electron transfer kinetics on mono- and multilayer graphene *ACS Nano* **8** 10089–100
- [24] Randviir E P, Brownson D A, Gomez-Mingot M, Kampouris D K, Iniesta J and Banks C E 2012 Electrochemistry of Q-graphene *Nanoscale* **4** 6470–80
- [25] Brownson D A C, Varey S A, Hussain F, Haigh S J and Banks C E 2014 Electrochemical properties of CVD grown pristine graphene: monolayer- vs. quasi-graphene *Nanoscale* **6** 1607–21
- [26] Güell A G, Cuharuc A S, Kim Y-R, Zhang G, Tan S-Y, Ebejer N and Unwin P R 2015 Redox-dependent spatially resolved electrochemistry at graphene and graphite step edges *ACS Nano* **9** 3558–71
- [27] Ping J, Vishnubhotla R, Xi J, Ducos P, Saven J G, Liu R and Johnson A T C 2018 All-electronic quantification of neuropeptide–receptor interaction using a bias-free functionalized graphene microelectrode *ACS Nano* **12** 4218–23
- [28] Heller I, Janssens A M, Männik J, Minot E D, Lemay S G and Dekker C 2008 Identifying the mechanism of biosensing with carbon nanotube transistors *Nano Lett.* **8** 591–5
- [29] Schedin F, Geim A K, Morozov S V, Hill E W, Blake P, Katsnelson M I and Novoselov K S 2007 Detection of individual gas molecules adsorbed on graphene *Nat. Mater.* **6** 652–5
- [30] Dankerl M *et al* 2010 Graphene solution-gated field-effect transistor array for sensing applications *Adv. Funct. Mater.* **20** 3117–24
- [31] Lin C-T, Loan P T K, Chen T-Y, Liu K-K, Chen C-H, Wei K-H and Li L-J 2013 Label-free electrical detection of DNA hybridization on graphene using Hall effect measurements: revisiting the sensing mechanism *Adv. Funct. Mater.* **23** 2301–7
- [32] Gui E L *et al* 2007 DNA sensing by field-effect transistors based on networks of carbon nanotubes *J. Am. Chem. Soc.* **129** 14427–32
- [33] Balasubramanian K, Burghard M and Kern K 2008 Effect of the electronic structure of carbon nanotubes on the selectivity of electrochemical functionalization *Phys. Chem. Chem. Phys.* **10** 2256–62
- [34] Mannik J, Goldsmith B R, Kane A and Collins P G 2006 Chemically induced conductance switching in carbon nanotube circuits *Phys. Rev. Lett.* **99** 016601
- [35] Deshmukh M M, Prieto A L, Gu Q and Park H 2003 Fabrication of asymmetric electrode pairs with nanometer separation made of two distinct metals *Nano Lett.* **3** 1383–5
- [36] Unwin P R, Güell A G and Zhang G 2016 Nanoscale electrochemistry of sp<sup>2</sup> carbon materials: from graphite and graphene to carbon nanotubes *Acc. Chem. Res.* **49** 2041–8
- [37] Bergveld P 2003 Thirty years of ISFETOLOGY: what happened in the past 30 years and what may happen in the next 30 years *Sensors Actuators B* **88** 1–20
- [38] Kaisti M 2017 Detection principles of biological and chemical FET sensors *Biosens. Bioelectron.* **98** 437–48
- [39] Janata J 2012 Graphene bio-field-effect transistor myth *ECS Solid State Lett.* **1** M29–31
- [40] Park K, Kang H, Koo S, Lee D and Ryu S 2019 Redox-governed charge doping dictated by interfacial diffusion in two-dimensional materials *Nat. Commun.* **10** 4931
- [41] Boussaad S, Diner B A and Fan J 2008 Influence of redox molecules on the electronic conductance of single-walled carbon nanotube field-effect transistors: application to chemical and biological sensing *J. Am. Chem. Soc.* **130** 3780–7
- [42] Narayanan R, Yamada H, Marin B C, Zaretski A and Bandaru P R 2017 Dimensionality-dependent electrochemical kinetics at the single-layer graphene–electrolyte interface *J. Phys. Chem. Lett.* **8** 4004–8
- [43] Cline K K, McDermott M T and McCreery R L 1994 Anomalous slow electron transfer at ordered graphite electrodes: influence of electronic factors and reactive sites *J. Phys. Chem.* **98** 5314–9
- [44] Iost R M, Crespilho F N, Zuccaro L, Yu H K, Wodtke A M, Kern K and Balasubramanian K 2014 Enhancing the electrochemical and electronic performance of CVD-grown graphene by minimizing trace metal impurities *ChemElectroChem* **1** 2070–4
- [45] Bard A J and Faulkner L R 2000 *Electrochemical Methods: Fundamentals and Applications* (New York: Wiley)
- [46] Shinwari M W, Zhitomirsky D, Deen I A, Selvaganapathy P R, Deen M J and Landheer D 2010 Microfabricated reference electrodes and their biosensing applications *Sensors* **10** 1679–715
- [47] Larrimore L, Nad S, Zhou X, Abruña H and McEuen P L 2006 Probing electrostatic potentials in solution with carbon nanotube transistors *Nano Lett.* **6** 1329–33

- [48] Chen P and McCreery R L 1996 Control of electron transfer kinetics at glassy carbon electrodes by specific surface modification *Anal. Chem.* **68** 3958–65
- [49] Palazzo G, De Tullio D, Magliulo M, Mallardi A, Intranuovo F, Mulla M Y, Favia P, Vikholm-Lundin I and Torsi L 2015 Detection beyond Debye's length with an electrolyte-gated organic field-effect transistor *Adv. Mater.* **27** 911–6
- [50] Gao N, Zhou W, Jiang X, Hong G, Fu T-M and Lieber C M 2015 General strategy for biodetection in high ionic strength solutions using transistor-based nanoelectronic sensors *Nano Lett.* **15** 2143–8
- [51] Jiang L, Fu W, Birdja Y Y, Koper M T M and Schneider G F 2018 Quantum and electrochemical interplays in hydrogenated graphene *Nat. Commun.* **9** 793
- [52] Macedo L J A, Lima F C D A, Amorim R G, Freitas R O, Yadav A, Iost R M, Balasubramanian K and Crespihlo F N 2018 Interplay of non-uniform charge distribution on the electrochemical modification of graphene *Nanoscale* **10** 15048–57
- [53] Sarkar S, Bekyarova E, Niyogi S and Haddon R C 2011 Diels–Alder chemistry of graphite and graphene: graphene as diene and dienophile *J. Am. Chem. Soc.* **133** 3324–7
- [54] Paulus G L, Wang Q H and Strano M S 2013 Covalent electron transfer chemistry of graphene with diazonium salts *Acc. Chem. Res.* **46** 160–70
- [55] Mann J A, Rodríguez-López J, Abruña H D and Dichtel W R 2011 Multivalent binding motifs for the noncovalent functionalization of graphene *J. Am. Chem. Soc.* **133** 17614–7
- [56] Brett C M A, Inzelt G and Kertesz V 1999 Poly(methylene blue) modified electrode sensor for haemoglobin *Anal. Chim. Acta* **385** 119–23
- [57] Brownson D A C, Gorbachev R V, Haigh S J and Banks C E 2012 CVD graphene vs. highly ordered pyrolytic graphite for use in electroanalytical sensing *Analyst* **137** 833–9
- [58] Yang W, Ratinac K R, Ringer S P, Thordarson P, Gooding J J and Braet F 2010 Carbon nanomaterials in biosensors: should you use nanotubes or graphene? *Angew. Chem. Int. Ed.* **49** 2114–38
- [59] Kang X, Wang J, Wu H, Aksay I A, Liu J and Lin Y 2009 Glucose oxidase–graphene–chitosan modified electrode for direct electrochemistry and glucose sensing *Biosens. Bioelectron.* **25** 901–5
- [60] Bartlett P N and Al-Lolage F A 2018 There is no evidence to support literature claims of direct electron transfer (DET) for native glucose oxidase (GOx) at carbon nanotubes or graphene *J. Electroanal. Chem.* **819** 26–37
- [61] Hirose A, Kasai T, Koga R, Suzuki Y, Kouzuma A and Watanabe K 2019 Understanding and engineering electrochemically active bacteria for sustainable biotechnology *Bioresour. Bioprocess.* **6** 10
- [62] Manohar S K, Fafadia C, Saran N and Rao R 2008 Faradaic effects in all-organic transistors *J. Phys. D: Appl. Phys.* **103** 094501
- [63] Singh M, Holzinger M, Tabrizian M, Winters S, Berner N C, Cosnier S and Duesberg G S 2015 Noncovalently functionalized monolayer graphene for sensitivity enhancement of surface plasmon resonance immunosensors *J. Am. Chem. Soc.* **137** 2800–3
- [64] Bunimovich Y L, Shin Y S, Yeo W-S, Amori M, Kwong G and Heath J R 2006 Quantitative real-time measurements of DNA hybridization with alkylated nonoxidized silicon nanowires in electrolyte solution *J. Am. Chem. Soc.* **128** 16323–31
- [65] Kwon S S, Shin J H, Choi J, Nam S and Park W I 2017 Defect-mediated molecular interaction and charge transfer in graphene mesh-glucose sensors *ACS Appl. Mater. Interfaces* **9** 14216–21